Planetary and Space Science 153 (2018) 142–156

Contents lists available at ScienceDirect

Planetary and Space Science

journal homepage: www.elsevier.com/locate/pss

Global and local re-impact and velocity regime of ballistic ejecta of boulder craters on Ceres

F. Schulzeck [a,*], S.E. Schröder [a], N. Schmedemann [b], K. Stephan [a], R. Jaumann [a], C.A. Raymond [c], C.T. Russell [d]

[a] German Aerospace Center (DLR), Berlin, Germany
[b] Freie Universität Berlin, Berlin, Germany
[c] Jet Propulsion Laboratory, California Institute of Technology, Pasadena, CA, USA
[d] UCLA, Los Angeles, CA, USA

A B S T R A C T

Imaging by the Dawn-spacecraft reveals that fresh craters on Ceres below 40 km often exhibit numerous boulders. We investigate how the fast rotating, low-gravity regime on Ceres influences their deposition. We analyze size-frequency distributions of ejecta blocks of twelve boulder craters. Global and local landing sites of boulder crater ejecta and boulder velocities are determined by the analytical calculation of elliptic particle trajectories on a rotating body. The cumulative distributions of boulder diameters follow steep-sloped power-laws. We do not find a correlation between boulder size and the distance of a boulder to its primary crater. Due to Ceres' low gravitational acceleration and fast rotation, ejecta of analyzed boulder craters (8–31 km) can be deposited across the entire surface of the dwarf planet. The particle trajectories are strongly influenced by the Coriolis effect as well as the impact geometry. Fast ejecta of high-latitude craters accumulate close to the pole of the opposite hemisphere. Fast ejecta of low-latitude craters wraps around the equator. Rotational effects are also relevant for the low-velocity regime. Boulders are ejected at velocities up to 71 m/s.

1. Introduction

Boulders on planetary surfaces are widely studied, because they provide insight into impact processes and the composition of the upper layer of the planetary body. Ballistic models are widely used to describe ejecta emplacement across a planetary surface as well as the material exchange between planetary bodies.

Large ejecta blocks have been identified with imagery of NASA's Dawn spacecraft around morphologically fresh craters (Schröder et al., 2016). In 2015, NASA's Dawn spacecraft arrived at the dwarf planet Ceres to investigate its surface and interior. Onboard instruments include a Gamma Ray and Neutron Detector (GRaND), a framing camera (FC) and a visible and infrared mapping spectrometer (VIR) (Russell and Raymond, 2011). In contrast to pre-Dawn models, mission data suggests that Ceres' heavily cratered crust consists of a ice-rock mixture with less than 40% ice (Bland et al., 2016). VIR data indicates a mixture of ammonia-bearing phyllosilicates, magnesium-bearing phyllosilicates and carbonates (De Sanctis et al., 2016). Ceres exhibits a wide morphologic variety of craters, but basins larger than 300 km are absent (Hiesinger et al., 2016). Furthermore, H_2O was detected, indicating water ice exposure (e.g. Combe et al., 2016). Floor fractured craters, large scale linear structures and domes are interpreted to be an indication for cryovolcanism (Buczkowski et al., 2016; Ruesch et al., 2016).

There are various analytical and numerical studies about the ballistic emplacement of ejecta on bodies of the Solar System. Particle trajectory models provide insight into the correlation between ejecta and existing structures and formations, such as grooves on Phobos (e.g. Davis et al., 1981; Nayak and Asphaug, 2016; Wilson and Head, 2015) and the Moon (Wieczorek and Zuber, 2001), secondary craters (Bierhaus et al., 2012), magnetic anomalies on the Moon (Hood and Artemieva, 2008), tektites on Mars (Lorenz, 2000; Wrobel, 2004) and lunar rays (Giamboni, 1959). Furthermore, ejecta emplacement models provide explanations about observed ejecta geometries and hence the impact process itself, such as for Hale crater on Mars (Schultz and Wrobel, 2012) and Chicxulub crater on Earth (Alvarez, 1996). Studies on global trajectory regimes, the fate of ejected particles and the transfer of particles between planetary bodies, especially between planets and their satellites, have been conducted to examine the interaction between planetary bodies (e.g. Alvarellos et al., 2002; Gladman et al., 1995; Nayak et al., 2016).

Boulders have been investigated with various points of focus, depending on the planetary body and the available data. Size-frequency distributions and shapes of boulders have been studied on the Moon (e.g.

* Corresponding author. Rutherfordstr. 2, Berlin, 12489, Germany.
E-mail address: franziska.schulzeck@dlr.de (F. Schulzeck).

https://doi.org/10.1016/j.pss.2018.02.004
Received 20 November 2017; Received in revised form 10 January 2018; Accepted 10 February 2018
Available online 13 February 2018
0032-0633/

Greenhagen et al., 2016; Krishna and Kumar, 2016), Mars (e.g. Di et al., 2016b; Golombek et al., 2003), satellites (e.g. Martens et al., 2015; Thomas et al., 2000), comets (e.g. Pajola et al., 2015), but especially on asteroids (e.g. Chapman et al., 2002; Jiang et al., 2015; Lee et al., 1996; Mazrouei et al., 2014; Michikami et al., 2008; Nakamura et al., 2008). Ejection velocities and in some cases ejection sites were estimated for the Moon (Bart and Melosh, 2010a, 2010b; Vickery, 1986), Eros (Durda et al., 2012; Thomas et al., 2001), Lutetia (Küppers et al., 2012) and Ida (Geissler et al., 1996). On Ceres, trajectories of ejection particles have been calculated numerically to test the correlation between ejecta emplacement and linear structures on the surface (Schmedemann et al., 2017).

The purpose of this study is to provide an overview about the ballistic emplacement of ejecta on Ceres, especially for smaller boulder craters. The criteria for the selected twelve boulder craters are the number of boulders, boulder diameters and the crater location. Selected craters must have enough identifiable boulders at a given resolution. Only six craters have enough large blocks that allow size measurements in a sufficient large diameter range. Additional craters were selected to cover all occurring boulder crater diameters and latitudes. At first, we mapped and, if possible, measured boulders of selected craters to analyze their distribution. Initially, we focused on the emplacement of all ejected particles. How do rotation and gravitational acceleration affect ejecta transport of craters in the diameter range of boulder craters? Subsequently, we wanted to know at which velocities boulders were ejected and how their trajectories were influenced by rotation. In addition, we investigate how the choice of impactor parameters alters resulting ejection velocities. We chose a fast and easy implemented analytical approach to calculate re-impact sites introduced by Dobrovolskis (1981).

2. Methods

2.1. Measurement and analysis of boulder and crater diameters

Boulder locations, boulder diameters and the diameters of unnamed craters were measured using the ArcGIS Add-In CraterTools (Kneissl et al., 2011), which allows the determination of diameters of circular features independent of image and data frame map projections. Measurements were conducted on mosaics based on data from Dawn's Low-Altitude-Mapping Orbit (LAMO) with a resolution of 35 m/pixel (Roatsch et al., 2016). Because of the non-circular outline of boulder craters, several circles were fitted to each crater to find average values for diameter and location of unnamed craters. Like boulder craters, boulders are of irregular shape and therefore the longest observable elongation of a block was used to define its diameter. Boulders larger than ~100 m could be distinguished morphologically. Close to the resolution limit, positive and negative topographic features can only be identified by the direction of the shadows they cast. We estimate the error for size measurements to be up to one pixel, which correspondents to 35 m. The separation of single boulders was additionally complicated by dense clustered blocks. In consequence, we decided that only measurements above ~100 m object size are reliable and were therefore used for interpretation. In addition, we identify the largest boulders for 30 craters on Ceres to compare the relation between the maximum block size and the crater diameter.

To analyze the linear relation between block distances and block diameters, we calculated the correlation coefficient, using the Scipy statistics package (Oliphant, 2007). The correlating coefficient *coeff* is defined as $coeff = \sum xy / \sqrt{\sum x^2 \sum y^2}$, with $x = x_i - \overline{x}$ and $y = y_i - \overline{y}$, in which $\overline{x}$ and $\overline{y}$ are the mean values (e.g. Bewick et al., 2003). Coefficients close to ±1 indicate a strong positive or negative linear relationship. Coefficients close to 0 indicates no linear relationship (e.g. Vo.T.H et al., 2017). We decided not to derive p-values for a null hypothesis test that is used to test the significance of the correlation, because a larger number of data points is recommended.

2.2. Size-frequency distributions

Rock fragmentation has been shown to follow a power-law behavior (Hartmann, 1969). Power-law distributions are widely used to describe boulder distributions (e.g. DeSouza et al., 2015; Li et al., 2017; Michikami et al., 2008) and were therefore fitted to our diameter data sets. To fit the distribution, estimating uncertainties and plot results, we use a Matlab implementation of the statistical methods described in Clauset et al. (2009). Closely following their description, a data series follows a power-law distribution, if it satisfies the probability distribution $p(x) \propto x^{-\alpha}$, where α is the exponent or scaling factor. We have a continuous data set, whose complementary cumulative distribution function (CCDF) $P(x)$ is defined by equation (1).

$$P(x) = \int_x^\infty p(x')dx' = \left(\frac{x}{x_{min}}\right)^{-1+\alpha} \quad (1)$$

The lower bound of the power-law behavior is described by x_{min}. Maximum likelihood estimators are used to fit the power-law distribution to the data set. The lower cutoff of the scaling region is estimated with the goodness-of-fit method, based on Kolmogorov-Smirnov statistics. Uncertainties for the constants x_{min} and α are calculated as well.

Goodness-of-fit tests provide so-called p-values (not the same p-value as in statistical hypothesis testing in section 2.1), which describe whether the hypothesis of a power-law distribution is suitable. For this purpose, the "distance" between the data and the model is calculated. That deviation is compared to distances of synthetic data sets. The p-value is the fraction of synthetic data sets that has a larger distance than the empirical ones. It takes values between 0 and 1. Values close to 1 indicate that the model is a good fit for the data. Discrepancies arise from statistical fluctuations. A rule-of-thumb threshold for a good fit is 0.1. Values below that threshold indicate that the power-law distribution is not a good fit for the data. If the number of samples is low, the test is not reliable. To rule out power-law behavior, a large number (~>100) of samples is needed for the p-value to fall off below the threshold.

Sometimes, rock fragmentation is also described by the Weibull distribution (stretched exponential) (Weibull, 1951). It is used, for instance, to describe the size distribution of volcanic ashes (e.g. Gouhier and Donnadieu, 2008). Because of its characteristic rollover at smaller sizes it can be well suited to describe the size-frequency distribution of secondary craters (Ivanov, 2006; Werner et al., 2009) and can therefore be applicable for ejecta blocks as well. We focus on power-law fits because they are more commonly used to describe the size distribution of ejecta blocks and therefore make our results comparable. Nevertheless, we tested whether a stretched exponential distribution would be a better fit for our data with a likelihood ratio test (Clauset et al., 2009). We used the implementation by Alstott et al. (2014). If that ratio is sufficiently positive, the first distribution is considered to be the better fit, if negative the second one. Another p-value is introduced to describe the significance of such ratios. The chosen threshold for the second p-value is 0.1. For values above the threshold, no statement about a favored model can be made.

2.3. Scaling laws

Impact crater scaling laws defined by theory and laboratory experiments describe the relationship between impactor, target and the resulting impact crater (Werner and Ivanov, 2015). For a detailed derivation analysis, we refer to Ivanov (2001) and Werner and Ivanov (2015). The transient crater diameter is the diameter of the initial cavity before crater modification sets in (Melosh and Ivanov, 1999). The transient crater diameter for complex craters is defined as $D_t = D_{sc}^{0.15} D^{0.85}$ (Croft, 1985) and for simple craters as $D_t \approx D/1.25$ (Werner and Ivanov, 2015). D is the crater diameter and D_{sc} is the simple-to-complex transition diameter. On Ceres, Hiesinger et al. (2016) calculated a simple-to-complex transition diameter of 10.3 km. Holsapple (1993) distinguishes between strength and gravity regime. The choice of regime

depends on the size of the impactor. The strength regime applies to smaller projectiles and is used if the crustal strength of the target is large compared to the lithostatic pressure. On the contrary, the surface gravity dominates in the gravity regime. Schmidt and Housen (1987) define a scaling law, which describes the relationship between projectile size and the transient crater diameter. The scaling law uses the π-theorem (Buckingham, 1914), which puts parameters in dimensionless groups ("pi-groups") (Dowling and Dowling, 2013). Schmidt and Housen (1987) distinguish between two target scenarios: nonporous, zero friction rocks and dry friction material, such as sand. The relation between projectile diameter D_p and crater size for nonporous, zero friction rocks in equation (2) incorporates the strength-to-gravity transition (Ivanov, 2008; Neukum and Ivanov, 1994; Schmidt and Housen, 1987).

$$D_p = D_t \cdot \frac{\left(g\, D_t + D_{sg}\right)^{0.282}}{\left\{1.16\, \left(\frac{\delta}{\sigma}\right)^{\frac{1}{3}} \left(v_p \sin\alpha\right)^{0.44}\, g^{-0.22}\right\}^{\frac{1}{0.78}}} \tag{2}$$

Parameters that are incorporated in the projectile diameter equation are the strength-to-gravity transition diameter $D_{sg} = 1.75$ km (Hiesinger et al., 2016), the density of the projectile δ, the density of the target σ, the projectile velocity v_p and the impact angle of the projectile α.

Housen et al. (1983) introduced scaling laws for the ejection velocity of a particle $v(x)$ as a function of its distance x to the crater center. Richardson et al. (2005) adapted that equation for a gravity-dominated regime by allowing the velocity to drop to zero at the crater rim (equation (3)).

$$v(x) = \frac{2\sqrt{gR_t}}{(1+e_x)} \left(\frac{x}{R_t}\right)^{-e_x} - \frac{2\sqrt{gR_t}}{(1+e_x)} \left(\frac{x}{R_t}\right)^{\lambda} \tag{3}$$

R_t is the transient crater radius and e_x and λ are constants. The constant e_x is a material parameter and π-scaling results range from 1.8 for competent rock and 2.6 for quartz sand (Melosh, 1989). Housen et al. (1983) found a value of 2.44 of e_x for impacts into Ottawa sand. The value of λ is to be chosen between 6 and 10 (Richardson et al., 2005). Based on experimental (e.g. Anderson et al., 2003; Anderson et al., 2004; Cintala et al., 1999; Schultz et al., 2005) and numerical studies (Collins and Wünnemann, 2007), after Richardson (2007), in first-order approximation, the ejection angle φ with respect to the local surface horizontal is decreasing linearly with distance x from the impact center: $\varphi = \varphi_0 - \varphi_d\left(\frac{x}{R_t}\right)$. Following experimental results by Cintala et al. (1999), we use a starting angle $\varphi_0 = 52°$ and a dropping angle $\varphi_d = 18°$. An oblique impact, with an impact angle $\alpha < 90°$ with the respect to the surface horizontal, leads to decreasing ejection angles and increasing ejection velocities on the down-range side, which is defined as the opposite direction to the incoming projectile. The final ejection angle φ_L is given by equation (4).

$$\varphi_L = \varphi - \left[30° \left(\cos\alpha\right)\left(\frac{1-\cos\theta}{2}\right)\left(1-\frac{x}{R_t}\right)^2\right] \tag{4}$$

The particle's azimuth is θ. The resulting ejection velocity v_L is given in equation (5).

$$v_L = \left[\left(v\, sin\varphi\right)^2 + \left(v\frac{sin\varphi}{tan\varphi_L}\right)^2\right]^{\frac{1}{2}} \tag{5}$$

Oblique impacts are common; 45° is the most likely impact angle (Shoemaker, 1962), and is therefore used as a default value. Other default values (Table 1) are an impact velocity of 4.79 km/s, which is the average impact velocity for Ceres (O'Brien and Sykes, 2011), a target density of 1815 kg/m^3, which is in the range reported in Park et al. (2016) and an impactor density of dense rock (3000 kg/m^3) (Collins et al., 2005). North (azimuth $\theta = 0°$) was chosen as the default incoming direction of the impact. We use the value $e_x = 2.44$ derived for impacts into Ottawa sand by Housen et al. (1983), and the material constant $\lambda = 10$ according to Bart and Melosh (2010a) for a lunar setting, in the absence of better constrained material constants for Ceres.

We vary not well-constrained input parameters, such as the incoming direction, impacting angle and velocity of the projectile, the material constants e_x and λ and the densities of target and projectile to test their effect on resulting re-impact sites and velocities. In addition to the default incoming direction, projectiles impacting from south and west are tested as well as a low impact angle of 10° and a vertical impact of 90°. The average impact velocity is 4.79 km/s, but a majority of impacts have velocities below or above and only a small fraction of all impacts in the main belt and on Ceres show velocities above 8 km/s (O'Brien and Sykes, 2011). We test a low (2 km/s) and a high (8 km/s) impact velocity, related to impact probabilities on Ceres. We test different projectile materials, such as ice (1000 kg/m^3), porous rock (1500 kg/m^3) and iron (8000 kg/m^3) (Collins et al., 2005). In addition, we vary the target density by applying the lower (1680 kg/m^3) and upper bounds (1950 kg/m^3) for the density of Ceres' outer shell (Park et al., 2016).

2.4. Elliptical trajectories

We calculated elliptical orbits using fundamental equations for ballistic trajectories described in detail in Morris (1964). The ejection velocity of an elliptical orbit is based on three equations: the conservation of angular momentum $rv\cos(\vartheta) = \sqrt{\mu p} = const.$, where r is the magnitude of the radius vector from the center of the planetary body, v the velocity, ϑ the flight-path angle, μ the product of the gravitational acceleration, and the square of the body's radius and p the semilatus rectum. Secondly, the conservation of energy in terms of the vis-viva equation $v^2 = \mu\,(2/r - 1/a)$, with a as the semimajor axis of the elliptical orbit. Thirdly, the equation of the ellipse $1/r = (1 + \varepsilon\cos(\upsilon))/p$, where ε is the eccentricity and υ the true anomaly. The final range as a function of the ejection velocity is described in equation (6). It is the result of subtracting the true anomaly at the launch from the true anomaly at the terminal, where φ_L is the launch angle, v_L the launch velocity, and $\Delta\phi = f/R_P$ the ratio between the projected range on the surface of the body f and the planet radius R_P.

$$\Delta\phi = 2\mathrm{acos}\left(\frac{1 - v_L^2\cos^2(\varphi_L)}{\varepsilon}\right) = 2\mathrm{atan}\left(\frac{v_L^2\sin(\varphi_L)\cos(\varphi_L)}{1 - v_L^2\cos^2(\varphi_L)}\right) \tag{6}$$

2.5. Global and local re-impact regime on a rotating body

The Coriolis effect acts on particles that move relative to the rotating planetary body. It has a horizontal and a vertical component with respect to the planetary surface. The vertical component leads to a westward deflection of particles ejected upward. That westward deflection is at its maximum at the equator and zero at the poles. Horizontal moving particles in the northern hemisphere are deflected to the right of their original direction of motion. Due to the clockwise rotation, eastward moving particles are deflected towards the equator and westward moving particles to the poles. In the southern hemisphere, the effect of the horizontal component deflects particles to the left of their path. This effect also is latitude-dependent, finds its maximum at the poles and is not

Table 1
Default input parameters.

Parameter	Value
Impact angle α	45°
Incoming impact direction θ	0° N
Ejecion angle φ_L	45°
Projectile density δ	3000 kg/m^3
Projectile Velocity v_P	4.79 km/s
Target density σ	1815 kg/m^3
e_x	2.44
λ	10

Thrud

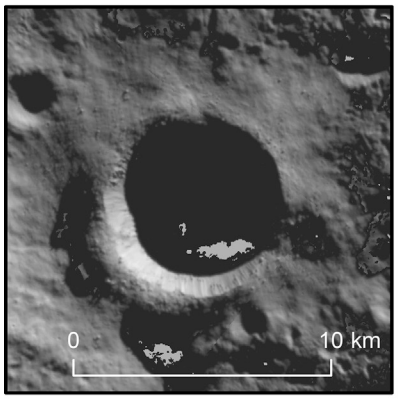

Crater A

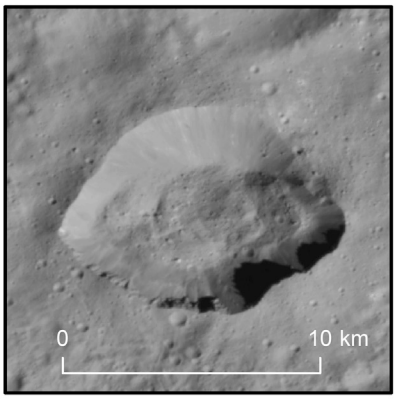

Braciaca

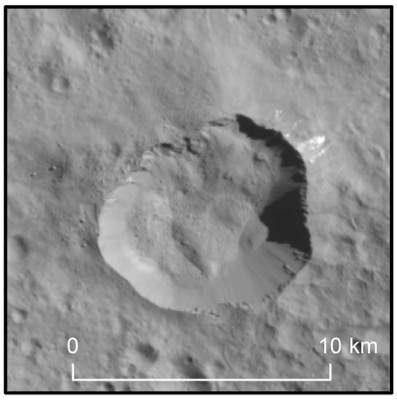

Crater B

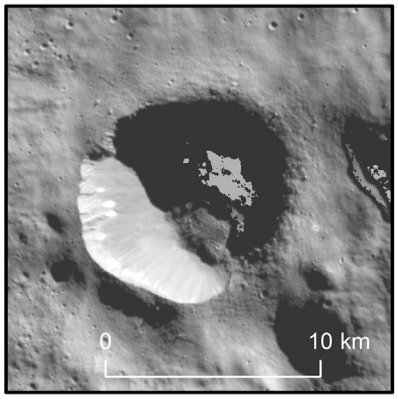

Oxo

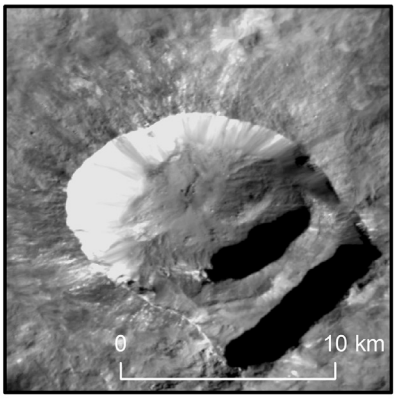

Cacaguat

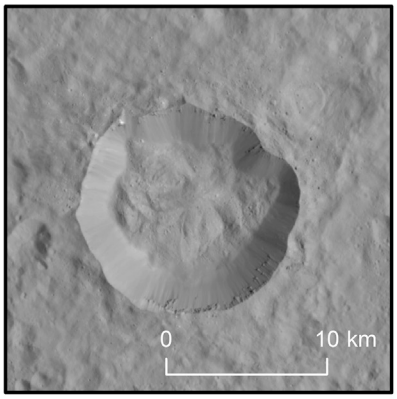

Crater C

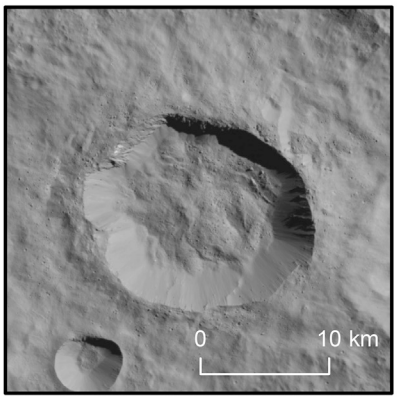

Crater D

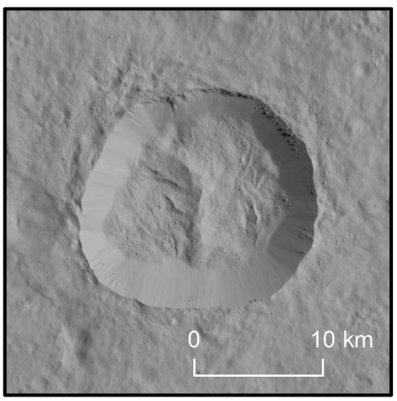

Ratumaibulu

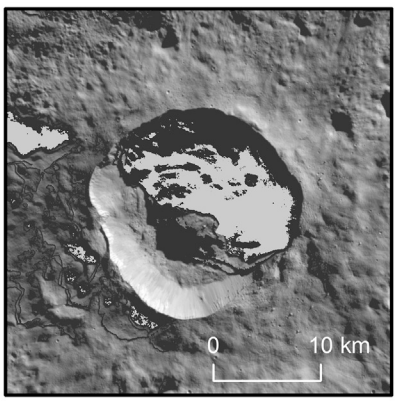

Juling

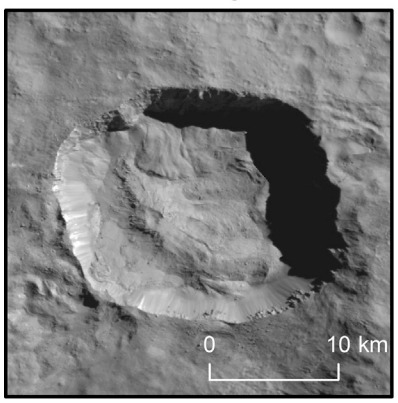

Nunghui

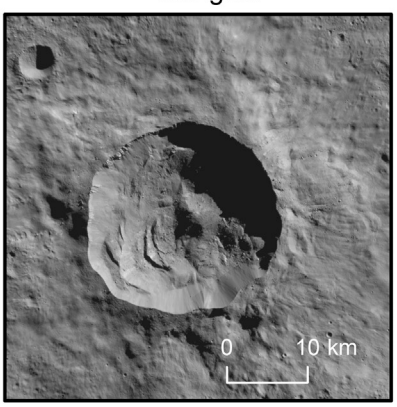

Jacheongbi

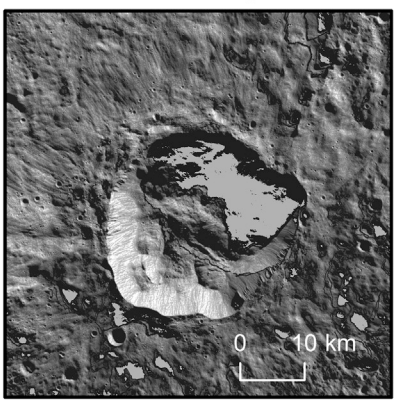

continued on next page

existent at the equator (e.g. Chow, 2013). We determine global re-impact sites of ejecta particles according to their ejection velocity on a rotating sphere by following an analytical approach described in Dobrovolskis (1981). For a detailed description of all calculations, we refer to the original publication. Calculations are based on the assumption of a spherical symmetric rigid body. The assumption is feasible for Ceres, since its shape is nearly spheroidal (Park et al., 2016). Atmospheric influences are neglected. Dimensionless units are used to simplify calculations. To describe the ballistic emplacement of a point mass relative to the rotating system, the eastward rotational velocity of Ceres is added to the particle's launch velocity. Ceres' dimensionless eastward angular velocity $\omega = 0.247$ at the time of the launch given by $= 3.3\ \mathrm{hr}/\sqrt{\rho}P$, with an orbital period of $P = 9.074$ h (Thomas et al., 2005) a bulk density of $\rho = 2.162\ \mathrm{kg}/m^3$ (Park et al., 2016). In addition, we use a mean radius $R = 476$ km and a gravitational acceleration of $g = 0.28\ \mathrm{m/s^2}$ (Thomas et al., 2005). The rotational component that is added to the eastward component of the particle's inertial velocity is then a product of the angular velocity and the sine of the start colatitude of the particle. We distributed ejection sites of test particles in a ring on a sphere. The ring resembles the area between the test crater's projectile radius and the transient crater radius.

To relate ejection velocities to specific boulder locations, incorporating the planet's rapid rotation, we used the Octave (Eaton et al., 2015) implementation of the Delaunay triangulation (Barber et al., 1996) to find the analytically calculated particle landing sites that are closest to the mapped boulder locations.

We think that due to the craters' richness in mass wasting features, it is unlikely that boulders inside the craters today are located where they were first deposited. Instead, the majority probably was moved by landslides and other processes of crater collapse. Therefore, we only use boulders outside the crater rim for velocity analyses.

3. Results

3.1. Crater morphology and boulder distribution

We morphologically analyze twelve selected craters between 7.8 and 31 km with large ejecta blocks, which provide a selection of boulder crater latitudes and crater diameters (Fig. 1). Coordinates and diameters are listed in Table 2. The projectile sizes, calculated with equation (2) are listed in Table 3. Size measurements are performed for six craters that have enough large ejecta blocks.

Most of the analyzed craters are located on Ceres' southern hemisphere. All craters feature a continuous ejecta layer and display multiple mass wasting features. Some craters exhibit shadowed areas due to poor illumination conditions during data acquisition, while others have permanently shadowed regions (Schorghofer et al., 2016), hence; not all interior structures are visible. Most of the investigated craters do not fit easily in the simple or complex crater scheme. Platz et al. (2016) distinguish between simple, modified simple, transitional complex and complex craters on Ceres. Thrud (7.8 km) is a perfectly simple bowl-shaped crater with a circular rim and steep crater walls. The rim of Crater B (9.6 km) is also nearly circular, but the crater floor is flatter than the crater floor of Thrud. The craters Oxo, Braciaca, Juling, Cacaguat, Crater A, Crater C and Crater D are characterized as transitional complex craters. They have scalloped rims and flat floors. Those craters are also characterized by lobate deposits in their interior. Such deposits can cover possible interior features. Oxo crater (10 km) has only one large terrace. Crater D is shallow with a flat floor and a central ridge, which might not be due to central uplift but to the encounter of two landslides that piled up in the middle of the crater. Nunghui (22 km) shows all characteristics of a complex crater, such as a central peak, a scalloped rim, a flat floor and multiple terraces. Other complex craters are Ratumaibulu and Jacheongbi. They exhibit flat floors with central mounds and scalloped crater rims.

We observe boulders inside and outside of nearly 60 craters. Some display hundreds, whereas others have only a few ejecta blocks. Boulders outside craters are usually distributed in all directions within two crater radii. Particularly asymmetrical boulder distributions are found around Crater A, Juling and Oxo. The deposition of large ejecta blocks often occurs in clusters and linear arranged groups. In total, we map between 9 boulders outside the crater rim of Oxo and 389 at Jacheongbi, which also has the largest block with 394 ± 35 m. Fig. 2 illustrates some examples of large ejecta blocks.

In Fig. 3 and Fig. 4, we analyzed the relation between a boulder's diameter and its distance from the crater rim. Correlation coefficients for both single crater's diameters and boulder sizes outside the crater rim and for diameters and sizes of all measurements combined are below $< \pm 0.3$ (Table 4), which means that there is no, or just a very weak, linear relationship. Boulders with diameters below 200 m can be found at any range from the crater center. A few large examples, especially for Jacheongbi, seem to be restricted to the area close to the crater rim. The gap between ~0.7 and 0.9 crater radii for all craters is explained by the crater walls that lie within this range. Those crater walls are characterized by steep slopes and there are not many boulders deposited directly on them. There are, however, boulders sliding down the walls. Their tracks are clearly visible. Those blocks are not included in our analysis, because their location clearly changed after their first deposition. A comparison of crater diameters and the diameter of their largest (Fig. 5), with a correlation coefficient of 0.68 suggests a strong (Evans, 1996) positive linear correlation between these two observations.

3.2. Boulder size distribution

We fit and evaluate power-laws of six cumulative boulder diameter distributions. The goodness-of-fit results, described by the p-value, are presented in Table 5. The smallest diameter that is used for the fit is represented by the value of x_{min}. Those diameters lie between 127 and 167 m. Those values agree with our observation that small diameter ranges suffer from greater measurement errors and are more incomplete than larger diameter ranges. By excluding small diameters, the total amount of blocks that are used for fitting is reduced. Only Crater C, Crater D and Jacheongbi have more than 100 used boulders. The p-values for Crater C and Crater D fall under the threshold of 0.1; hence, the power-law does not sufficiently describe their cumulative diameter distribution. Four craters: Ratumaibulu, Juling, Nunghui and Jacheongbi have p-values that are larger than the threshold of 0.1. However, for the analysis of the first three craters, the number of data points is very small. Therefore the goodness-of-fit test is not reliable, since the p-value might fall off if more measurements were available. We report the results of power-law fitting for those examples, with the chance that power-law fits are not best suited. The slopes of the power-law fits, as shown in Fig. 6, lie between -4.4 ± 0.7 and -6.2 ± 1.5.

The likelihood ratio tests (Table 6) that compare the power-law fit with a stretched exponential fit show that neither distribution is the significantly better fit because the p-values are always above the threshold for all six craters. That is why we cannot rule out either of the proposed fragmentation process behaviors. Note that this might only be true for the present data set where small diameters are missing because of the limit of resolution.

Fig. 1. Twelve boulder craters on Ceres, ordered by size displayed as LAMO clear-filter mosaics (35 m/pixel) in equidistant (Crater A, Braciaca, Oxo, Cacaguat, Crater C, Crater D and Juling) and stereographic projection (Thrud, Crater B, Ratumaibulu, Nunghui, Jacheongbi). No data values are displayed in a 30% gray. Coordinates and diameters are listed in Table 2.

Table 2
Coordinates and crater diameters of investigated boulder craters.

Crater	Longitude [°]	Latitude [°]	Diameter [km]
Thrud	31	−71.3	7.8
Crater A	−4.3	33.9	7.8
Braciaca	84.4	−22.8	8
Crater B	−115.2	−67.2	9.6
Oxo	−0.4	42.2	10
Cacaguat	143.6	−1.2	13.6
Crater C	−80.9	−23	15.6
Crater D	21.1	−10	18.1
Ratumaibulu	77.5	−67.3	20
Juling	168.5	−35.9	20
Nunghui	−87.7	−54	22
Jacheongbi	2.3	−69.2	31

Table 3
Projectile diameters of investigated boulder craters.

Crater	Projectile Diameter [km]
Thrud	0.4
Crater A	0.4
Braciaca	0.4
Crater B	0.5
Oxo	0.5
Cacaguat	0.9
Crater C	1.1
Crater D	1.3
Ratumaibulu	1.4
Juling	1.4
Nunghui	1.6
Jacheongbi	2.2

3.3. Global velocity and re-impact scheme

Fig. 7 and Fig. 8 illustrate particle landing sites as a function of ejection velocities in different projections. Our analytical model predicts that high-speed ejecta can travel large distances while it is highly influenced by the rotation of Ceres. The particle distraction due to rotation effect is strongly latitude-dependent. High-velocity particles string out along nearly latitude parallel lines (Fig. 7). Fig. 8 illustrates landing locations as a function of particle ejection velocity on maps that are centered on the pole of the crater's opposite hemisphere. We see that for craters at higher latitudes, such as Thrud (−71°), Crater B (−67.2°), Ratumaibulu (−67.3°), Nunghui (−54) and Jacheogbi (−69.2), fast particles accumulate near the pole of the opposite hemisphere. On the other hand, craters closer to the equator, such as Cacaguat (−1.2°) and Crater D (−10°) have high-velocity particles that accumulate around the equator (Fig. 7). Furthermore, large fractions of the ejecta of craters in the equatorial region, such as Cacaguat, are deposited more or less symmetrically to the equator. Impact locations of particles with different ejection velocities overlap. In a non-rotating setting, particles are deposited radially in a range that correlates with their velocities, so, close to the crater there is a circle of low-velocity particles and so forth. In a rotating setting however, particles with different ejection velocities can re-impact within the same distance to their primary crater. Fig. 7 shows that particles approximately up to 0.3 km/s are still deposited radially to the crater. Then we observe areas where trajectories are bent, so that the particles change their direction of motion. In consequence, re-impact locations of high-velocity particles interact with re-impact locations of particles with lower ejection velocities.

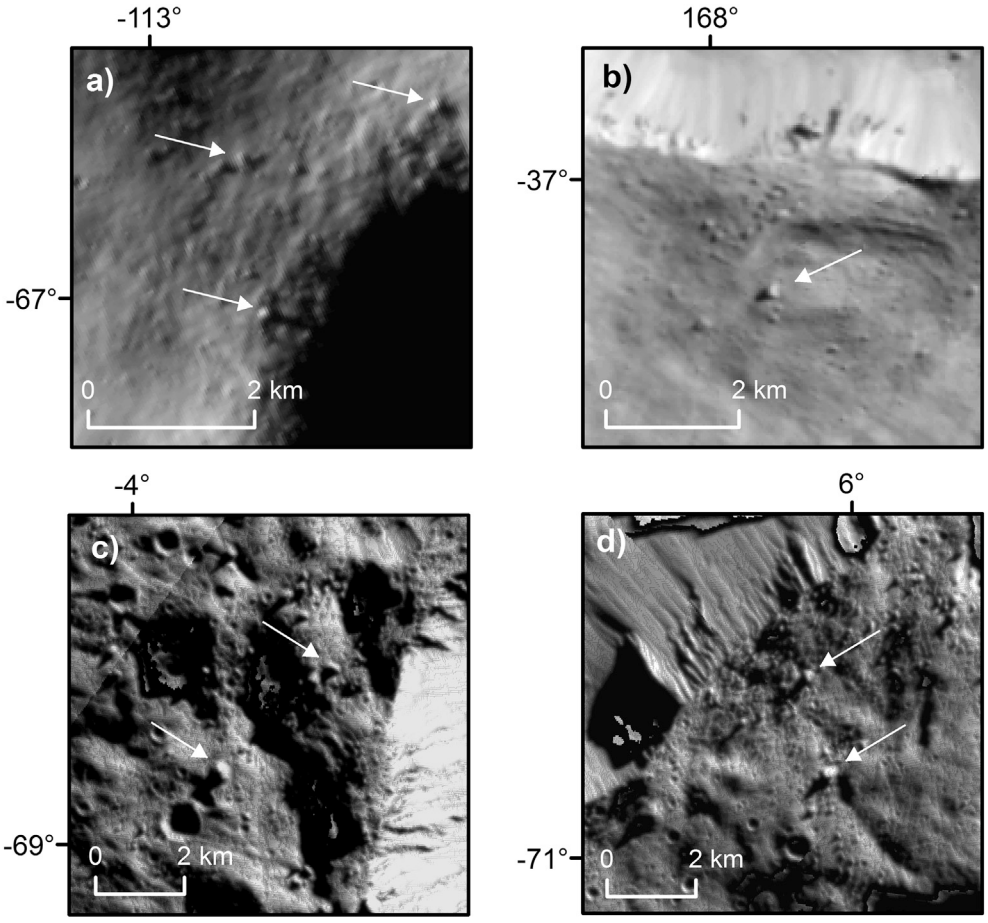

Fig. 2. Close-up view of boulders outside the crater rim of Crater B (a), Juling (b), and Jacheongbi (c, d). Note that there are some image artifacts close to the crater rim. White arrows mark selected example blocks.

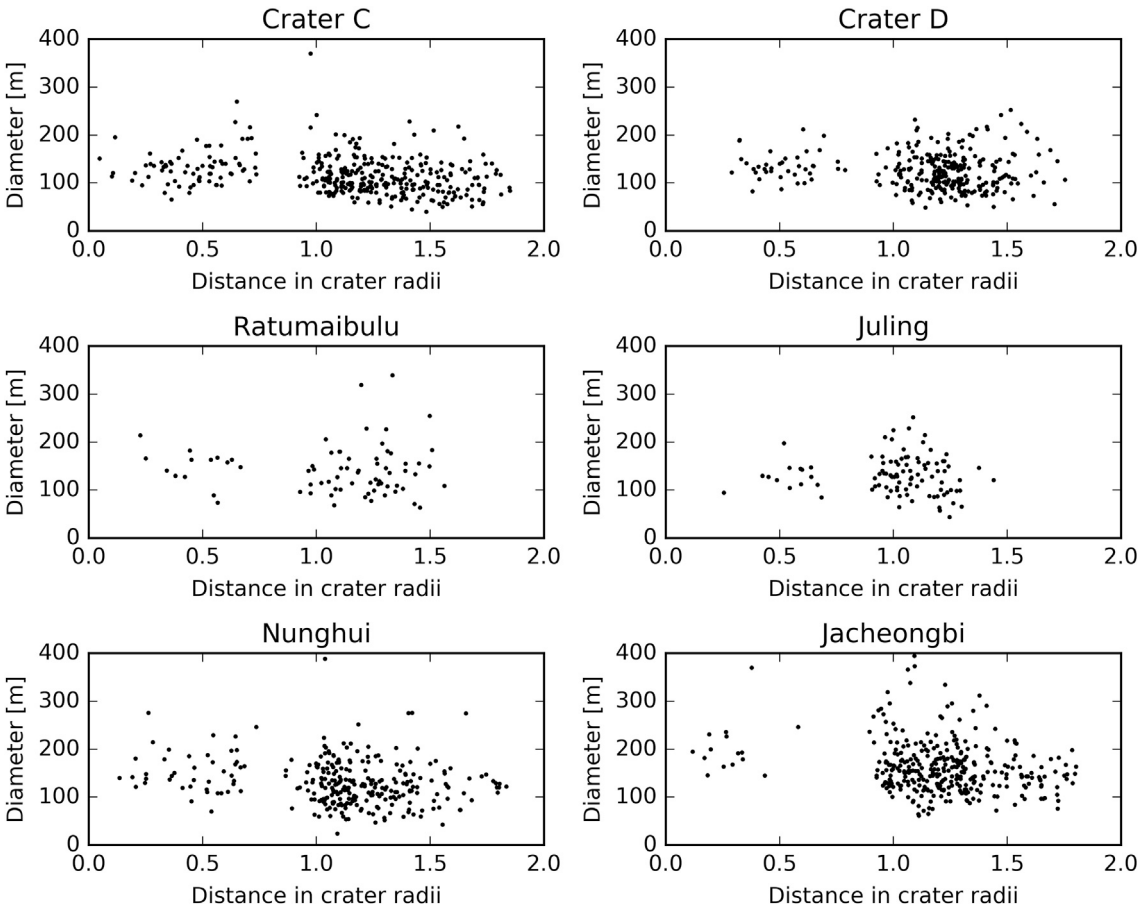

Fig. 3. Diameter measurements of ejecta blocks inside and outside six craters as a function of their distances to the crater center in radii of their parent crater.

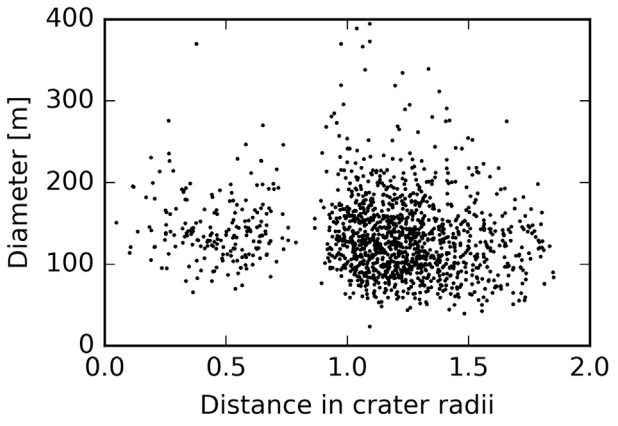

Fig. 4. Diameters measurements of ejecta blocks inside and outside of all six craters combined as a function of their distances to the crater center in radii of their parent crater.

3.4. The effect of input parameters on the global velocity and re-impact scheme

Impact conditions are, to some extent, unknown and cannot be specified by the crater's morphology. We tested the effect of input parameters on the resulting velocities and patterns as illustrated in Fig. 9. For the variation of parameters, we chose Crater D, because parameter variation can be illustrated best at an equatorial crater. For studying the local velocity regime, it is well-suited because of its fairly large size and the many identified boulder locations.

Table 4
Correlation coefficients evaluate the linear correlation between boulder size and its distance to the crater rim.

Crater	Correlation Coefficient
Crater C	−0.21
Crater D	0.01
Ratumaibulu	0.11
Juling	−0.21
Nunghui	−0.06
Jacheongbi	−0.19
All	0.23

The largest visible alteration of re-impact sites is produced by both the direction and the impact angle of the projectile. A change in the projectile's incoming direction causes large alterations in the re-impact regime (Fig. 9a–c). The impact angle changes the turnover point where particles start moving from east to west (Fig. 9d and e). Fig. 9a–d also illustrates the asymmetry in deposition that is caused by an oblique impact. In comparison with a vertical impact, as illustrated in Fig. 9e, high-velocity particles of an oblique impact (Fig. 9a–d) are distributed less symmetrically around the equator. For a 10° impact (Fig. 9d), for instance, particles change their direction of motion from east to west at different longitudes north and south of the equator. The calculation of the projectile radius and consequently start locations and velocities depend on the impactor velocity, target and projectile density. Compared to the impact geometry, the effect of material parameters and velocities on ejecta trajectories is less significant (Fig. 9f–l). On account of this, varying input parameters always influences the particles' trajectories, but the only major effects are caused by impact angle and direction.

Equation (3) describes the ejection velocity as a function of the

Table 5
Parameters for power-law fits of six craters. The goodness-of-fit test is described by the p-value with a threshold of at least 0.1 for a fit of sufficient quality. The test depends on a sample size that is large enough (~>100). The boldface marks the p-value that is above the threshold while using a large sample size. Ratumaibulu, Juling and Nunghui also have p-values above the threshold, but the number of data points is too low to evaluate the fit (in brackets). The minimum diameter that follows such a distribution is x_{min} and α the exponent of the power-law decay. The slope of the power-law fit is listed along with the number of used data points.

Crater	P-value	Alpha	Slope/Exponent (1 – alpha)	x_{min}	Blocks Mapped	Blocks used for Fitting
Crater C	0.008	6.1 ± 0.8	-5.1 ± 0.8	127.0 ± 13	353	120
Crater D	0.097	6.5 ± 1.4	$- 5.5 \pm 1.4$	134.8 ± 11.7	284	104
Ratumaibulu	(0.316)	5.6 ± 1.4	-4.6 ± 1.4	139.9 ± 14.6	71	36
Juling	(0.363)	6.7 ± 1.8	-5.7 ± 1.8	144.3 ± 14.5	96	34
Nunghui	(0.893)	7.2 ± 1.5	-6.2 ± 1.5	166.8 ± 21.9	282	58
Jacheongbi	**0.35**	5.4 ± 0.7	-4.4 ± 0.7	162.6 ± 16.7	336	147

Table 6
The power-law distribution is compared to a stretched exponential distribution. A sufficient positive or negative likelihood-ratio (LR) would make one or the other distribution a better fit. A p-value in the column next to the LR describes the significance of the latter. The threshold is chosen to be 0.1. Larger values indicate that no model is favored.

Crater	LR	P-value
Crater C	−0.62	0.55
Crater D	−2.66	0.14
Ratumaibulu	0.10	0.65
Juling	−0.53	0.49
Nunghui	0.16	0.65
Jacheongbi	−1.22	0.30

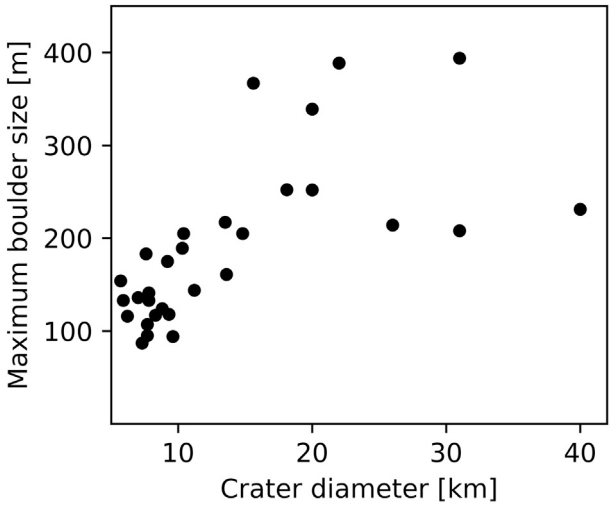

Fig. 5. Diameters of the largest boulders of 30 craters as a function of the crater diameter.

distance to the crater center. The constants e_x and λ resemble material properties, but literature provides only a limited number of material possibilities and constraints for planetary bodies. We calculated ejection velocities of Crater D with varying constants. Particles are ejected between projectile radius and transient crater radius. By varying the constant e_x by ± 10%, based on our default value of sand (Housen et al., 1983), we find that velocities increase with increasing e_x (Fig. 10). The effect is smaller below the escape velocity (Fig. 10 inset) and negligible for velocities below 100 m/s. We also varied λ between 6 and 10, but that choice does not affect the resulting velocities in any significant way.

3.5. Boulder ejection velocities

Our calculations show that boulders are ejected at comparably low velocities between 0.3 m/s (Juling) and 71 m/s (Jacheongbi), whereas the total range of velocities for particles that re-impact onto the surface is restricted by the escape velocity of 510 m/s. Fig. 11 illustrates ejection velocities as a function of the boulders' distances to the crater rim in crater radii. Ejection velocities decrease from the crater center to the crater rim. The flight paths of particles with higher ejection velocities are longer than those for low-velocity particles, which are deposited close to the outside of the crater rim. In addition, we observe that larger craters provide particles with higher velocities than smaller craters. The maximum ejection velocity for the smallest crater Thrud is 34 m/s, and the maximum velocity for the largest crater Jacheongbi is 71 m/s. Most boulders were mapped within a distance of 2 crater radii. Two exceptions are Oxo and Crater C, where ejecta blocks were found beyond. Just like for the global ejecta pattern, we tested the effect of different input variables on the resulting boulder velocities. In comparison with global ejection velocities, variations of projectile and target density, projectile velocity incoming direction and the incoming angle have almost no effect as illustrated for the impact angle and impact direction in Fig. 12. However, the vertical scenario (Fig. 12b) illustrates the rotational effect on low-velocity ejecta. A vertical impact in a rotating system results in velocity values that are slightly scattered around that curve due to rotation, because the particles are not any more symmetrically distributed around the crater.

Furthermore, we calculate the location of the corresponding launch sites to the ejecta blocks. Launch and landing sites of all twelve craters are illustrated in Fig. 13. The ejection sites of the ejecta blocks are mostly found at the outer edge of the crater floor, where low-velocity particles are ejected. The higher the initial velocity, the closer the launch location is to the crater center.

4. Discussion and conclusion

We study the influence of the fast rotation and low gravitational acceleration of the dwarf planet Ceres on the global and local (boulder) ejecta deposition pattern as a function of ejection velocity using an analytical approach.

Power-law size-frequency distributions of boulders on Ceres show steep slopes between −4.4 and −6.2. Not all craters' diameter distributions could be approximated by a power-law, because of their shape or too few data points. Using a variety of fitting techniques, steep power-law slopes of boulder diameter distributions are reported, for instance, for the Moon (e.g. Bart and Melosh, 2010a) and the asteroids Lutetia (Küppers et al., 2012), Eros (Chapman et al., 2002) and Toutatis (Jiang et al., 2015). Cumulative distributions of ejecta blocks and also of resulting secondary craters usually have a steeper slope than cumulative distributions of primary craters because of rock fragmentation (e.g. McEwen and Bierhaus, 2006; Shoemaker, 1965; Wilhelms et al., 1978).

Our model shows that ejected particles from small craters can travel over the entire surface of Ceres. The trajectories of high-velocity particles are bent to a great extent by the Coriolis effect. Particles that will reach such high velocities probably have a very low mass, and not all ejecta will fall back in form of secondary impacts, continuous ejecta and boulders. However, our results are important for the analysis of secondary craters, because they imply that those might be found far away from their primary crater and their line of sight will probably be not straight at all.

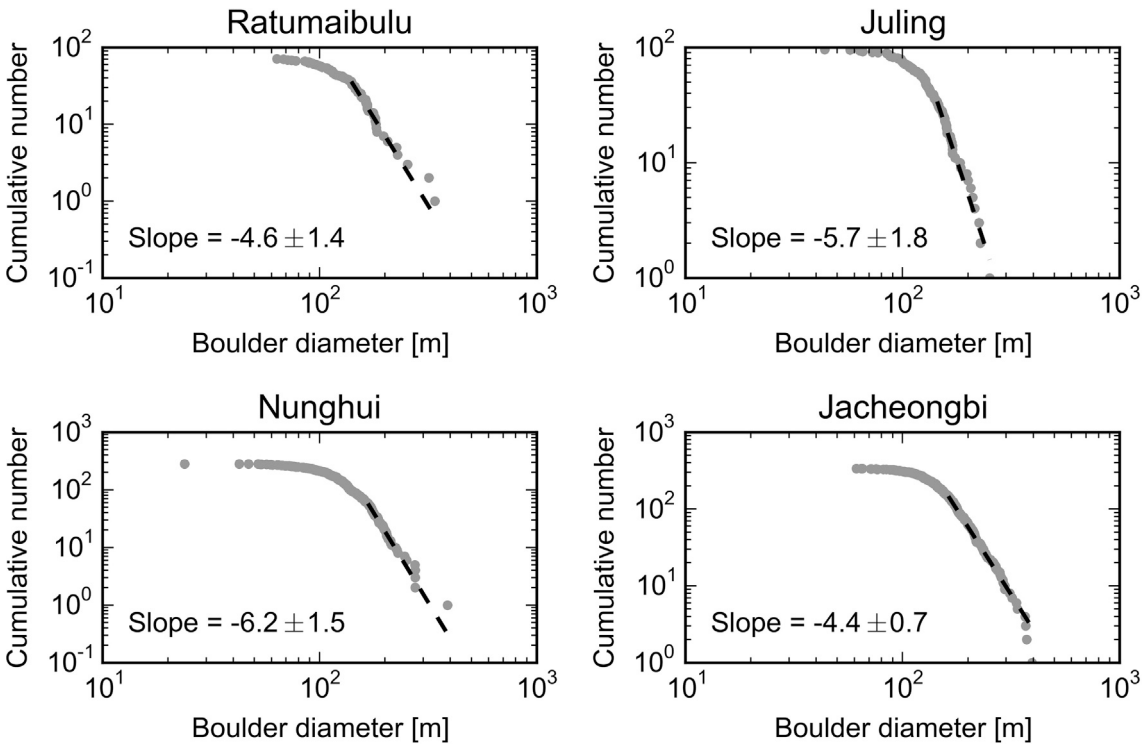

Fig. 6. Cumulative distribution of boulder diameters and slopes/exponents of power-law fits for four craters.

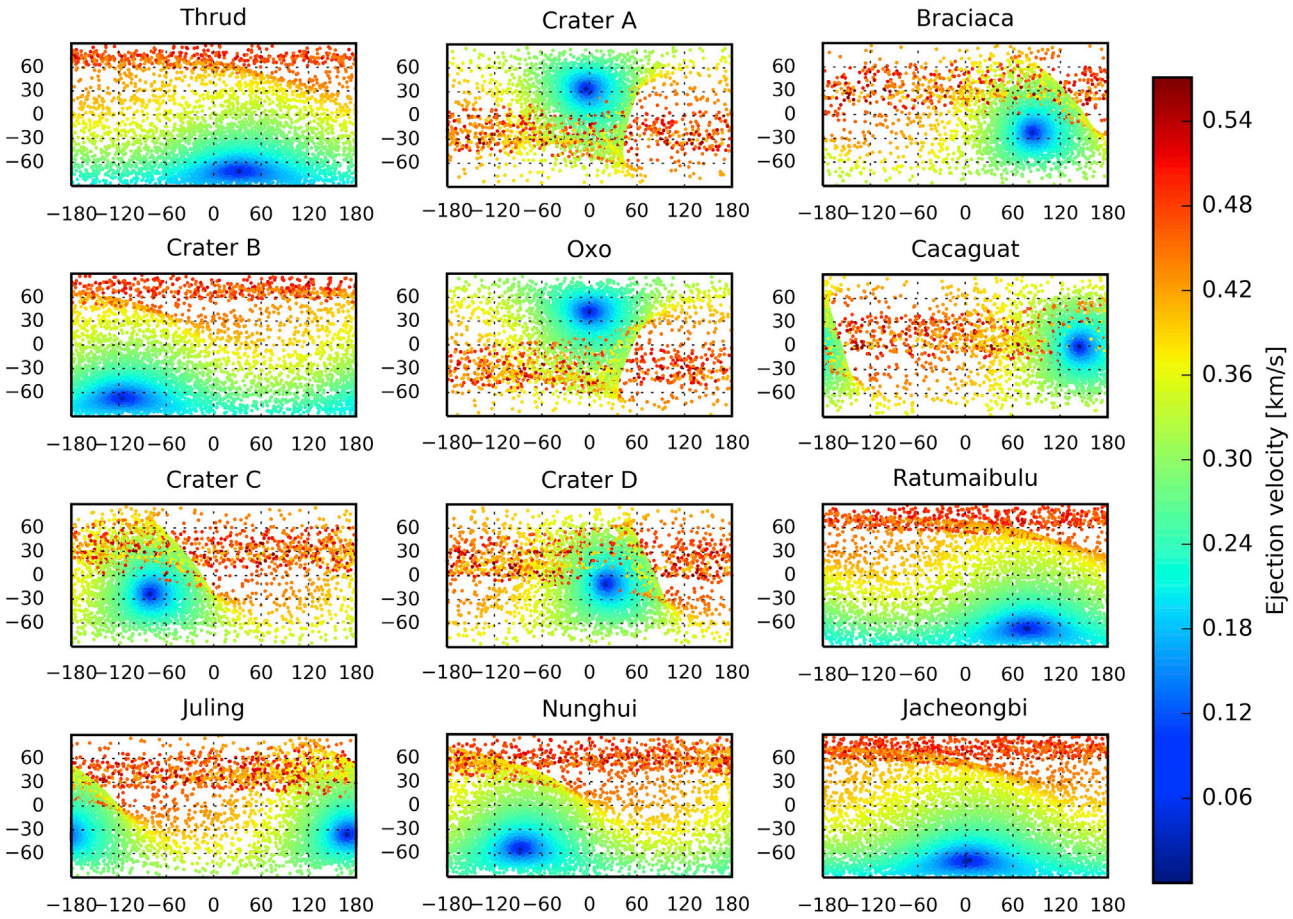

Fig. 7. Particle re-impact sites as a function of their ejection velocity. Maps are displayed in equirectangular projection. Note that particles might be faster than the escape velocity because the shown velocity is the velocity relative to the rotating body.

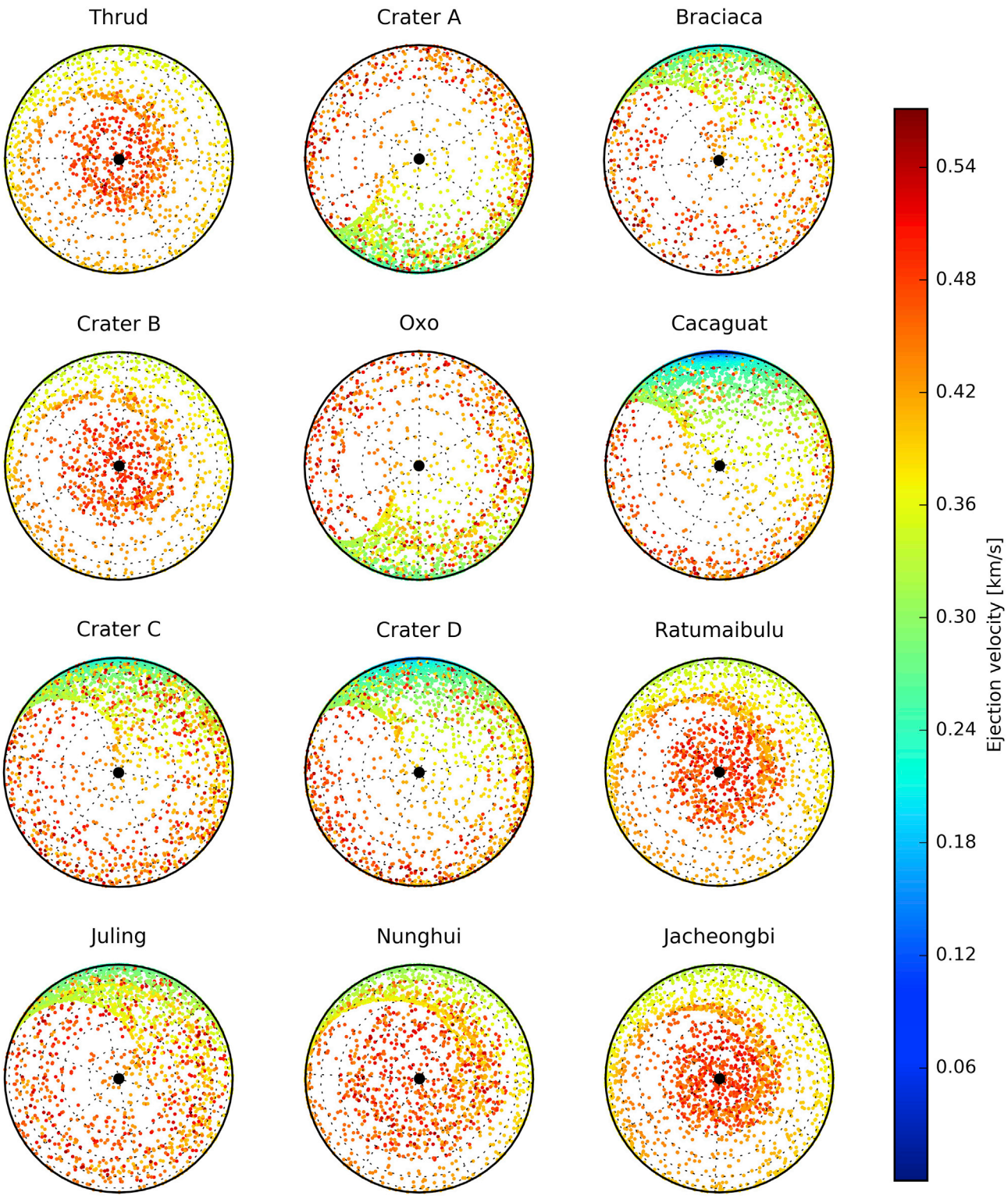

Fig. 8. Global re-impact pattern as a function of the particles' ejection velocity. The maps are in orthographic projection, centered at the pole of the crater's opposite hemisphere. The pole is marked by a black dot. Note that particles might be faster than the escape velocity because the shown velocity is the velocity relative to the rotating body.

Furthermore, we also show that the deposition of low-velocity fragments is influenced by rotation. In addition, as postulated by crater scaling laws, we observe a relationship between boulder velocity and its distance to the crater rim. Ejection velocities are proportional to the impactor's energy; hence, ejecta blocks of large craters reach higher velocities and are transported farther away from the crater rim. As a result, we provide a velocity range in which intact ejecta fragments can be expected.

Our observations of the rotational effect on ejecta deposition on Ceres are in good agreement with studies on other planetary bodies. For Mercury, Dobrovolskis (1981) reported that high-velocity particles string out along a circle of fixed latitude and that ejecta of impacts near the equator

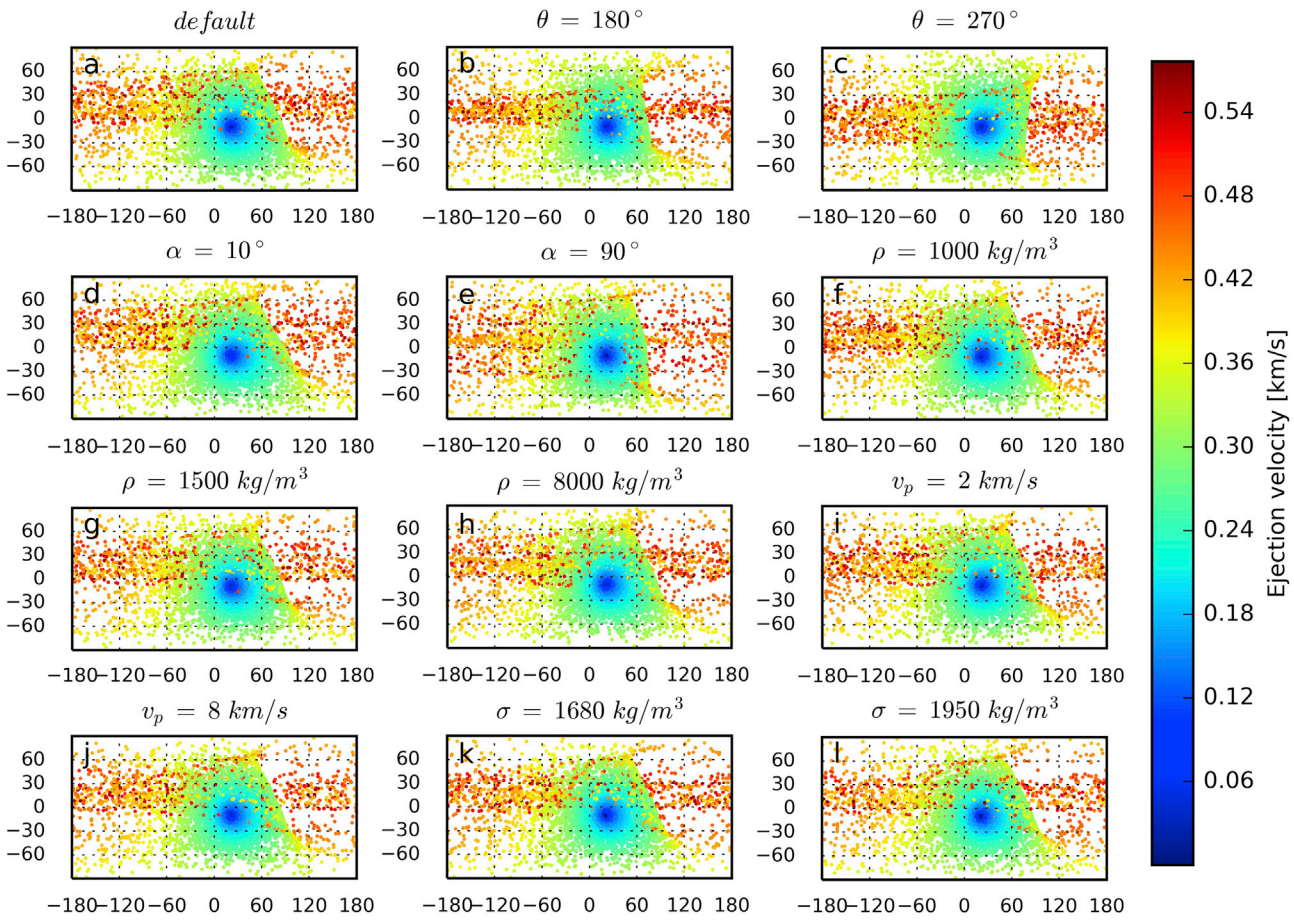

Fig. 9. Testing the effect of different input parameters on Crater D. a) An impact with the default values of a 45° impact angle with a projectile from the north (0° azimuth), an impact velocity of 4.79 km/s, a target density of 1815 kg/m^3 and an impactor density of dense rock (3000 kg/m^3). b) An impact with the incoming azimuth of 180° (south). c) An impact with the incoming azimuth of 270° (west). d) The projectile impacts with an angle of 10° with respect to the surface. e) The projectile impacts with an angle of 90° (vertical impact). f), g) and h) Different impactor materials: ice (1000 kg/m^3), porous rock (1500 kg/m^3) and iron (8000 kg/m^3). i) and j) Projectile velocities of 2 km/s and 8 km/s k) and l) Lowest and highest densities of Ceres outer layer (Park et al., 2016). Note that particles might be faster than the escape velocity because the shown velocity is the velocity relative to the rotating body.

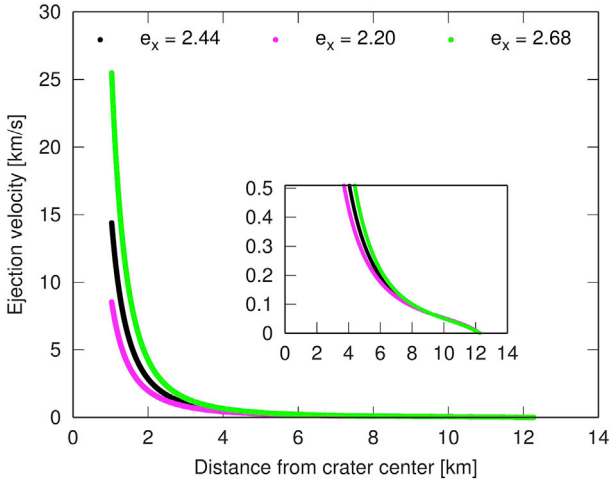

Fig. 10. We test the effect of the material parameter e_x on ejection velocities as a function of the particle's distance from the crater center. Our first choice of e_x is 2.44. The variable is varied ±10% to test its effect on resulting ejection velocities of Crater D. The other parameter λ is kept at 10. The inset shows velocities below Ceres' escape velocity of 0.51 km/s.

deposits symmetrically to the latter. High-velocity (distal) ejecta of high-latitude craters (>45°) on Mars tends to wrap poleward in the opposite hemisphere and equatorially for low-latitude craters (<45°) (Wrobel, 2004).

On the moon, boulder sizes decrease with increasing distance from the crater rim (Bart and Melosh, 2010a; Krishna and Kumar, 2016; Vickery, 1986). Based on that correlation, there is also a relation between ejection velocity and fragment size (Bart and Melosh, 2010a; Vickery, 1986). In addition, large fragments of large craters on the Moon are ejected at low velocities, whereas small craters do not show such correlation. However, we do not observe such trends in our data, only single observations agree with reported relations. The largest crater in our study is Jacheongbi, with a diameter of 31 km. Its largest boulders are indeed located close to the crater rim and would therefore have been ejected at lower velocities. Reasons for the absence of a relationship between boulder diameter and distance to the crater rim can be material properties in the upper layer, impact conditions and boulder transport mechanisms that might be different for Ceres. A more likely explanation is that the number and quality of data points is not sufficient. Boulder diameter measurements could only be performed for a few craters. We chose those craters that have many large boulders. Even then, some measurements are performed close to the limit of resolution and are not complete for any diameter range, because boulders can be covered by shadows and other boulders. A resolution of 35 m/pixel does not allow the exact measurement of meter-sized fragments. As a result, we think

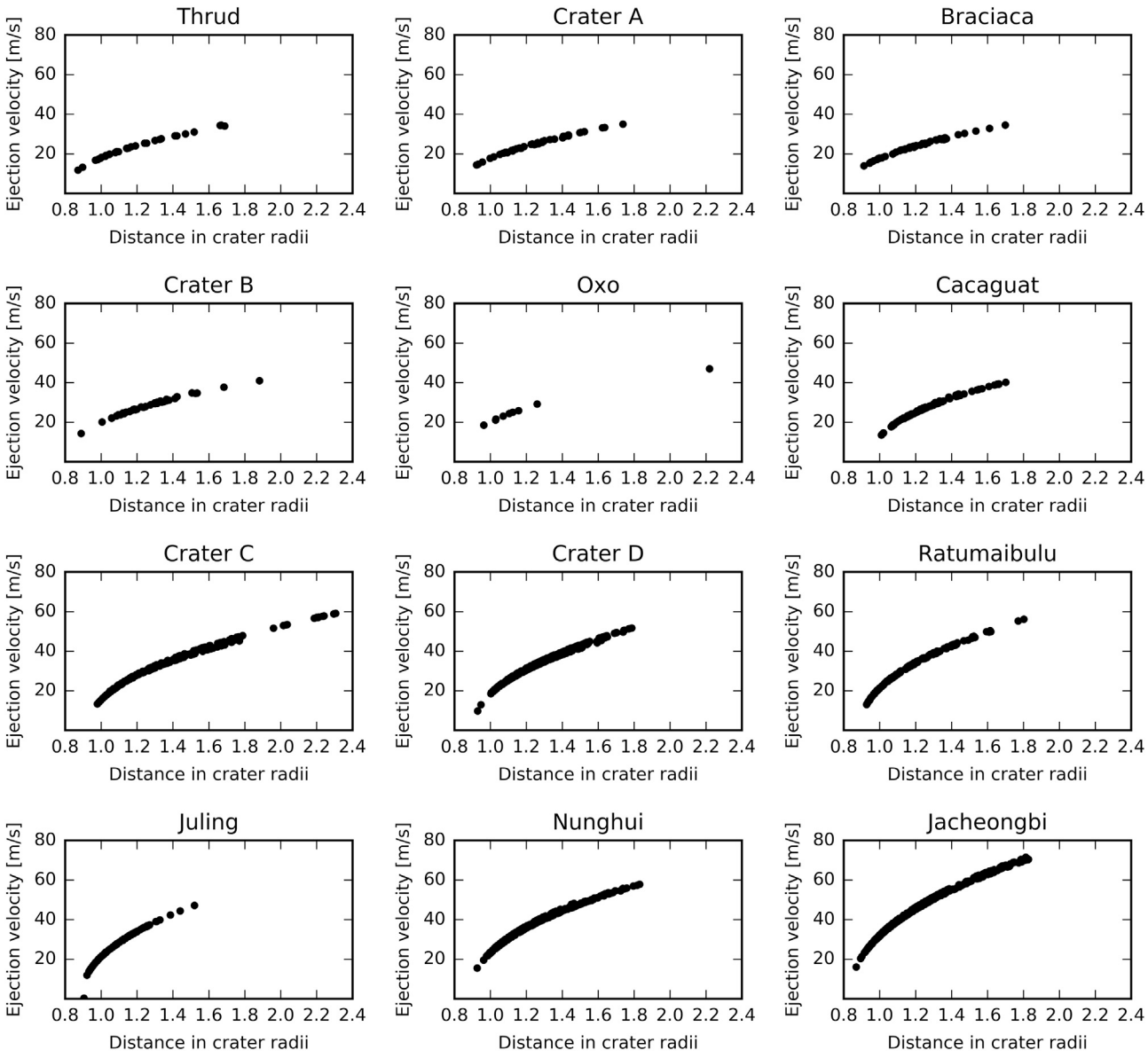

Fig. 11. Ejection velocities as a function of the radius of the parent crater, displayed for the boulders of twelve craters.

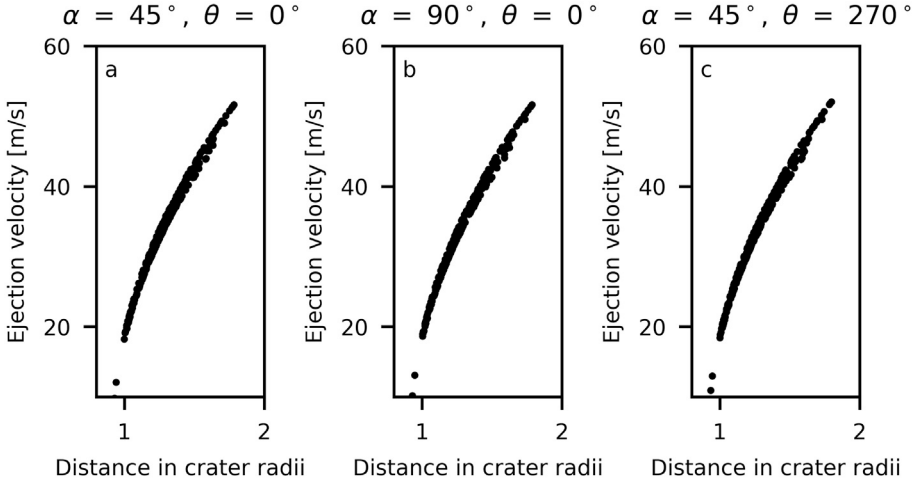

Fig. 12. The effect of the impacting angle and impact direction of the projectile on ejection velocities of boulders using the example of Crater D. a) The projectile hits the target with an angle of 45° with respect to the surface with an azimuth of 0°. b) The projectile hits the target with an angle of 90° with an azimuth of 0°. c) The projectile hits the target with an angle of 45° with an azimuth of 270°.

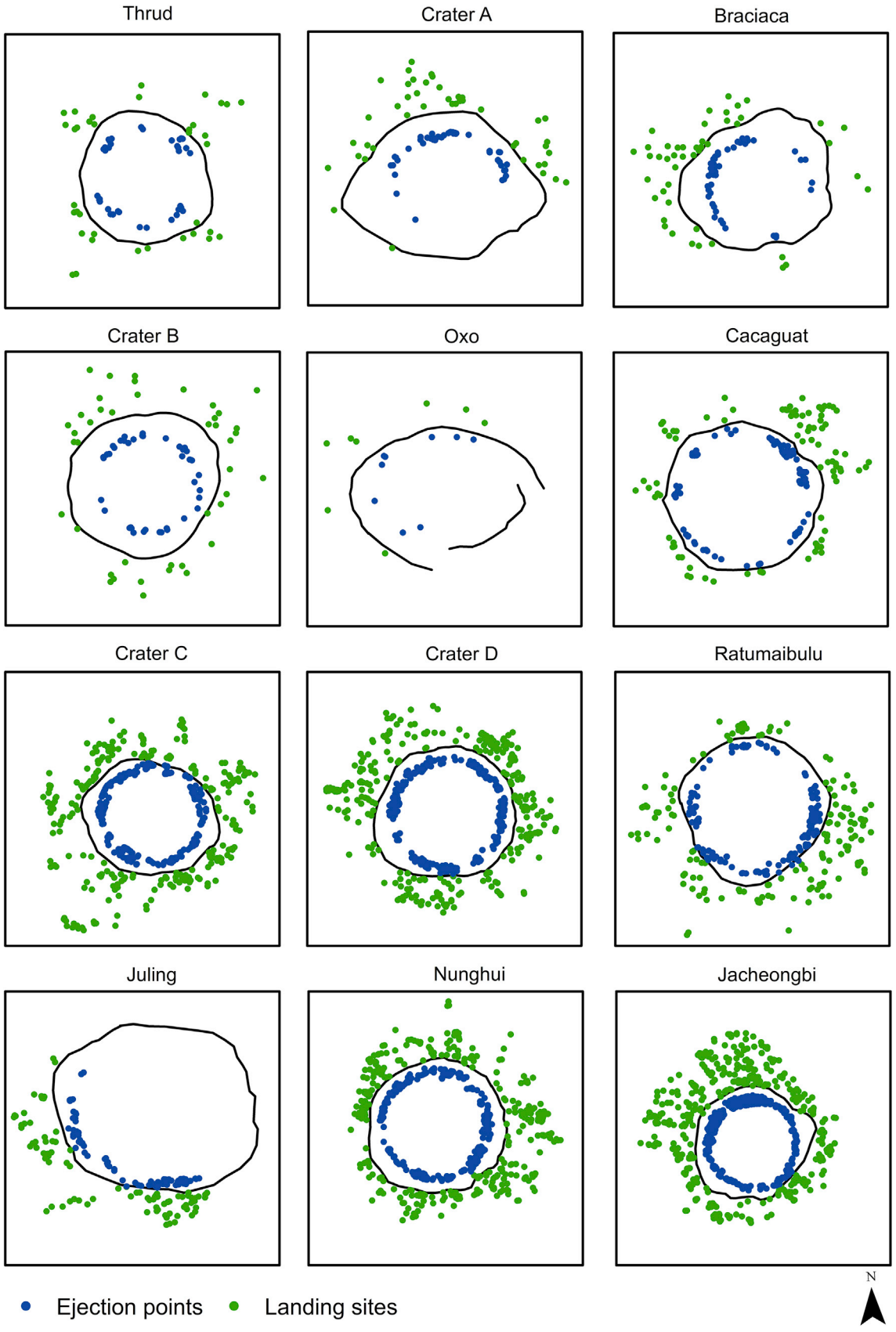

Fig. 13. Launch and landing sites of the boulders of twelve craters. Mapped boulder locations are displayed in green and corresponding ejection sites in blue. (For interpretation of the references to colour in this figure legend, the reader is referred to the Web version of this article.)

that such a correlation might exist, but can only be seen at higher resolution. By comparing the largest boulders of 30 craters, we find a positive linear correlation between crater size and the largest boulder. For craters below 20 km on the Moon, Phobos, Deimos and Ida, Lee et al. (1996) reported a power-law relationship between those two observations.

The input parameters that have a crucial effect on the distribution of re-impact sites are impact direction and impact angle, because they influence ejection angles and ejection velocities. We choose 45° as the most probable impact angle. The morphologies of the craters do not reveal the exact impact conditions, because only very oblique impacts (<5°) produce the characteristic "butterfly wing" pattern (Pierazzo and Melosh, 2000). A variation of the other input parameters velocity, projectile and target density do not change the final pattern much. However, the influence on single particle trajectories can be much larger. Parameters beside the impact angle and direction are direct inputs in the calculation of the projectile size. While the effect of those parameters on the projectile size is major, the resulting change in velocities and landing sites is small.

Scaling laws were derived from low-velocity laboratory experiments (Werner and Ivanov, 2015), and the materials used do not necessarily resemble the complex mineralogy of Ceres. Ceres' shallow subsurface consists of a mixture of ice (30–40%), rock, salts and/or clathrates (Bland et al., 2016). Prettyman et al. (2017) report surface materials that are rich in hydrogen, especially at mid-to-high latitudes, and have undergone aqueous alteration as seen in neutron and gamma-ray spectroscopy of the Dawn spacecraft that addresses decimeter scales of the shallow subsurface. They report about 10 wt % water ice in Ceres' ice table and a regolith porosity of 0.2. The thickness and exact composition of the regolith layer on Ceres is not well determined. If craters below <10 km in this study would have impacted into a thick silicate-rich regolith layer, a porous crater scaling might also be as realistic as a nonporous crater scaling.

Most of the examined craters are morphologically somewhat in between simple and complex, as discussed in section 3.1. Because the equations we used are based on the crater morphology, transient diameters sometimes can be under- or overestimated. The start locations of the identified boulders are highly dependent on the location of the crater center, the average crater diameter and the calculated transient crater diameter. Since most of the crater rims deviate considerably from a circular shape, the identification of the location of the center is difficult. As a result, some ejection sites are located at the crater wall, which is unrealistic.

The interpretation of our results will benefit from an overall study of secondary craters on Ceres and studies about the regolith thickness and boulder lifetimes. Size-frequency distributions of secondary craters can then be compared to the distribution of large ejecta blocks. Then again, we have shown that due to long-range particles, secondary craters might be a dominant feature on the surface, and their assignment to primary craters is challenging. Head et al. (2002) found that a regolith cover on Mars reduces ejection speeds. A similar relationship is reported for the Moon (Bart and Melosh, 2010b). However, the determination of regolith thickness by analyzing the morphological shape of small impact craters after an approach by Quaide and Oberbeck (1968) or by measuring regolith thickness directly from high-resolution DEM data (Di et al., 2016a) requires higher resolution.

For the first time, we analytically modeled re-impact sites of boulder crater ejecta and report ejection velocities for boulders on Ceres, taking into account its rapid rotation. Our results provide velocity limits in which intact ejecta fragments can be expected. We show that ejecta of small craters can travel long distances, and trajectories of high-velocity particles are bent to a great extent due to the Coriolis effect. Our results imply that Ceres' surface is largely contaminated with secondaries and that their assignment to specific craters is nearly impossible. Ceres' rotation even influences the trajectories of low-velocity fragments. Ejecta blocks are therefore not necessarily ejected radially.

Acknowledgments

We thank Stephanie Werner for reviewing the manuscript and providing helpful comments and suggestions. We also thank Sharon Uy for proofreading the manuscript. In addition, we thank the Dawn team for the development, cruise, orbital insertion, and operations of the Dawn spacecraft at Ceres. Dawn data are archived with the NASA Planetary Data System (http://sbn.pds.nasa.gov/).

References

Alstott, J., Bullmore, E., Plenz, D., 2014. Powerlaw: a Python package for analysis of heavy-tailed distributions. PLoS One 9, e85777.
Alvarellos, J.L., Zahnle, K.J., Dobrovolskis, A.R., Hamill, P., 2002. Orbital evolution of impact ejecta from Ganymede. Icarus 160, 108–123.
Alvarez, W., 1996. Trajectories of ballistic ejecta from the Chicxulub crater. In: Ryder, G., Fastovsky, D.E., Gartner, S. (Eds.), The Cretaceous-tertiary Event and Other Catastrophes in Earth History. Geological Society of America, pp. 141–150.
Anderson, J.L., Schultz, P.H., Heineck, J.T., 2003. Asymmetry of ejecta flow during oblique impacts using three-dimensional particle image velocimetry. J. Geophys. Res.: Plan 108.
Anderson, J.L., Schultz, P.H., Heineck, J.T., 2004. Experimental ejection angles for oblique impacts: implications for the subsurface flow-field. Meteoritics Planet Sci. 39, 303–320.
Barber, C.B., Dobkin, D.P., Huhdanpaa, H., 1996. The quickhull algorithm for convex hulls. ACM Trans. Math Software 22, 469–483.
Bart, G.D., Melosh, H.J., 2010a. Distributions of boulders ejected from lunar craters. Icarus 209, 337–357.
Bart, G.D., Melosh, H.J., 2010b. Impact into lunar regolith inhibits high-velocity ejection of large blocks. J. Geophys. Res.: Plan 115.
Bewick, V., Cheek, L., Ball, J., 2003. Statistics review 7: correlation and regression. Crit. Care 7, 451.
Bierhaus, E.B., Dones, L., Alvarellos, J.L., Zahnle, K., 2012. The role of ejecta in the small crater populations on the mid-sized saturnian satellites. Icarus 218, 602–621.
Bland, M.T., et al., 2016. Composition and structure of the shallow subsurface of Ceres revealed by crater morphology. Nat. Geosci. 9, 538–542.
Buckingham, E., 1914. On physically similar systems; illustrations of the use of dimensional equations. Phys. Rev. 4, 345–376.
Buczkowski, D.L., et al., 2016. The geomorphology of Ceres. Science 353.
Chapman, C.R., Merline, W.J., Thomas, P.C., Joseph, J., Cheng, A.F., Izenberg, N., 2002. Impact history of Eros: craters and boulders. Icarus 155, 104–118.
Chow, T.L., 2013. Classical Mechanics, second ed. CRC Press.
Cintala, M.J., Berthoud, L., Hörz, F., 1999. Ejection-velocity distributions from impacts into coarse-grained sand. Meteoritics Planet Sci. 34, 605–623.
Clauset, A., Shalizi, C.R., Newman, M.E., 2009. Power-law distributions in empirical data. SIAM Rev. 51, 661–703.
Collins, G., Wünnemann, K., 2007. Numerical modeling of impact ejection processes in porous targets. Lunar and Planetary Science Conference 38, 1789.
Collins, G.S., Melosh, H.J., Marcus, R.A., 2005. Earth Impact Effects Program: a Web-based computer program for calculating the regional environmental consequences of a meteoroid impact on Earth. Meteoritics Planet Sci. 40, 817–840.
Combe, J.P., et al., 2016. Detection of local H2O exposed at the surface of Ceres. Science 353.
Croft, S.K., 1985. The scaling of complex craters. Journal of Geophysical Research: Solid Earth 90, C828–C842.
Davis, D.R., Housen, K.R., Greenberg, R., 1981. The unusual dynamical environment of Phobos and Deimos. Icarus 47, 220–233.
De Sanctis, M.C., et al., 2016. Bright carbonate deposits as evidence of aqueous alteration on (1). Ceres. Nature 1–4.
DeSouza, I., Daly, M.G., Barnouin, O.S., Ernst, C.M., Bierhaus, E.B., 2015. Improved techniques for size–frequency distribution analysis in the planetary sciences: application to blocks on 25143 Itokawa. Icarus 247, 77–80.
Di, K., Sun, S., Yue, Z., Liu, B., 2016a. Lunar regolith thickness determination from 3D morphology of small fresh craters. Icarus 267, 12–23.
Di, K., et al., 2016b. Rock size-frequency distribution analysis at the Chang'E-3 landing site. Planet. Space Sci. 120, 103–112.
Dobrovolskis, A., 1981. Ejecta patterns diagnostic of planetary rotation. Icarus 47, 203–219.
Dowling, D.R., Dowling, T.R., 2013. Scaling of impact craters in unconsolidated granular materials. Am. J. Phys. 81, 875–878.
Durda, D.D., Chapman, C.R., Merline, W.J., Enke, B.L., 2012. Detecting crater ejecta-blanket boundaries and constraining source crater regions for boulder tracks and elongated secondary craters on Eros. Meteoritics Planet Sci. 47, 1087–1097.
Eaton, J.W., Bateman, D., Hauberg, S., Wehbring, R., 2015. GNU Octave Version 4.0.0 Manual: a High-level Interactive Language for Numerical Computations.
Evans, J.D., 1996. Straightforward Statistics for the Behavioral Sciences. Brooks/Cole.
Geissler, P., et al., 1996. Erosion and ejecta reaccretion on 243 Ida and its moon. Icarus 120, 140–157.
Giamboni, L.A., 1959. Lunar rays: their formation and age. Astrophys. J. 130, 324.
Gladman, B.J., Burns, J.A., Duncan, M.J., Levison, H.F., 1995. The dynamical evolution of lunar impact ejecta. Icarus 118, 302–321.
Golombek, M.P., et al., 2003. Rock size-frequency distributions on Mars and implications for Mars Exploration Rover landing safety and operations. J. Geophys. Res.: Plan 108.

Gouhier, M., Donnadieu, F., 2008. Mass estimations of ejecta from Strombolian explosions by inversion of Doppler radar measurements. J. Geophys. Res.: Solid Earth 113 n/a-n/a).
Greenhagen, B.T., et al., 2016. Origin of the anomalously rocky appearance of Tsiolkovskiy crater. Icarus 273, 237–247.
Hartmann, W.K., 1969. Terrestrial, lunar, and interplanetary rock fragmentation. Icarus 10, 201–213.
Head, J.N., Melosh, H.J., Ivanov, B.A., 2002. Martian meteorite launch: high-speed ejecta from small craters. Science 298, 1752–1756.
Hiesinger, H., et al., 2016. Cratering on Ceres: implications for its crust and evolution. Science 353.
Holsapple, K.A., 1993. The scaling of impact processes in planetary sciences. Annu. Rev. Earth Planet Sci. 21, 333–373.
Hood, L.L., Artemieva, N.A., 2008. Antipodal effects of lunar basin-forming impacts: initial 3D simulations and comparisons with observations. Icarus 193, 485–502.
Housen, K.R., Schmidt, R.M., Holsapple, K.A., 1983. Crater ejecta scaling laws: fundamental forms based on dimensional analysis. J. Geophys. Res.: Solid Earth 88, 2485–2499.
Ivanov, B., 2008. Size-frequency distribution of asteroids and impact craters: estimates of impact rate. In: Adushkin, V., Nemchinov, I. (Eds.), Catastrophic Events Caused by Cosmic Objects. Springer Netherlands, Dordrecht, pp. 91–116.
Ivanov, B.A., 2001. Mars/moon cratering rate ratio estimates. Space Sci. Rev. 96, 87–104.
Ivanov, B.A., 2006. Notes about secondary crater SFD. Planetary Chronology Workshop 6018.
Jiang, Y., Ji, J., Huang, J., Marchi, S., Li, Y., Ip, W.-H., 2015. Boulders on asteroid Toutatis as observed by Chang'e-2. Scientific reports. 5.
Kneissl, T., van Gasselt, S., Neukum, G., 2011. Map-projection-independent crater size-frequency determination in GIS environments—new software tool for ArcGIS. Planet. Space Sci. 59, 1243–1254.
Krishna, N., Kumar, P.S., 2016. Impact spallation processes on the Moon: a case study from the size and shape analysis of ejecta boulders and secondary craters of Censorinus crater. Icarus 264, 274–299.
Küppers, M., et al., 2012. Boulders on lutetia. Planet. Space Sci. 66, 71–78.
Lee, P., et al., 1996. Ejecta blocks on 243 Ida and on other asteroids. Icarus 120, 87–105.
Li, B., Ling, Z., Zhang, J., Chen, J., 2017. Rock size-frequency distributions analysis at lunar landing sites based on remote sensing and in-situ imagery. Planet. Space Sci. 146, 30–39.
Lorenz, R.D., 2000. Microtektites on Mars: volume and texture of distal impact ejecta deposits. Icarus 144, 353–366.
Martens, H.R., Ingersoll, A.P., Ewald, S.P., Helfenstein, P., Giese, B., 2015. Spatial distribution of ice blocks on Enceladus and implications for their origin and emplacement. Icarus 245, 162–176.
Mazrouei, S., Daly, M., Barnouin, O.S., Ernst, C., DeSouza, I., 2014. Block distributions on itokawa. Icarus 229, 181–189.
McEwen, A.S., Bierhaus, E.B., 2006. The importance of secondary cratering to age constraints on planetary surfaces. Annu. Rev. Earth Planet Sci. 34, 535–567.
Melosh, H., Ivanov, B., 1999. Impact crater collapse. Annu. Rev. Earth Planet Sci. 27, 385–415.
Melosh, H.J., 1989. Impact Cratering: a Geologic Process. Oxford University Press.
Michikami, T., et al., 2008. Size-frequency statistics of boulders on global surface of asteroid 25143 Itokawa. Earth Planets Space 60, 13–20.
Morris, D.N., 1964. Charts for Determining the Characteristics of Ballistic Trajectories in a Vacuum. RAND Corporation, Santa Monica, CA.
Nakamura, A., et al., 2008. Impact process of boulders on the surface of asteroid 25143 Itokawa—fragments from collisional disruption. Earth Planets Space 60, 7–12.
Nayak, M., Asphaug, E., 2016. Sesquinary catenae on the Martian satellite Phobos from reaccretion of escaping ejecta. Nat. Commun. 7.
Nayak, M., Nimmo, F., Udrea, B., 2016. Effects of mass transfer between Martian satellites on surface geology. Icarus 267, 220–231.
Neukum, G., Ivanov, B., 1994. Crater size distributions and impact probabilities on Earth from lunar, terrestrial-planet, and asteroid cratering data. Hazards due to Comets and Asteroids 359.
O'Brien, D.P., Sykes, M.V., 2011. The origin and evolution of the asteroid belt—implications for Vesta and Ceres. Space Sci. Rev. 163, 41–61.
Oliphant, T.E., 2007. Python for scientific computing. Computing in Science and Engg 9, 10–20.
Pajola, M., et al., 2015. Size-frequency distribution of boulders≥ 7 m on comet 67P/Churyumov-Gerasimenko. Astron. Astrophys. 583, A37.
Park, R.S., et al., 2016. A partially differentiated interior for (1) Ceres deduced from its gravity field and shape. Nature 537, 515.
Pierazzo, E., Melosh, H.J., 2000. Understanding oblique impacts from experiments, observations, and modeling. Annu. Rev. Earth Planet Sci. 28, 141–167.
Platz, T., et al., 2016. Impact cratering on Ceres: the simple-to-complex transition. Lunar and Planetary Science 2308.
Prettyman, T.H., et al., 2017. Extensive water ice within Ceres' aqueously altered regolith: evidence from nuclear spectroscopy. Science 355, 55–59.
Quaide, W.L., Oberbeck, V.R., 1968. Thickness determinations of the lunar surface layer from lunar impact craters. J. Geophys. Res. 73, 5247–5270.
Richardson, J.E., Melosh, H.J., Artemeiva, N.A., Pierazzo, E., 2005. Impact cratering theory and modeling for the deep impact mission: from mission planning to data analysis. Space Sci. Rev. 117, 241–267.
Richardson, J.E., Melosh, H.J., Lisse, C.M., Carcich, B., 2007. Aballistics analysis of theDeep Impact ejecta plume: Determining Comet Tempel 1's gravity, mass, anddensity. Icarus 191, 176–209.
Roatsch, T., et al., 2016. High-resolution Ceres high altitude mapping orbit atlas derived from Dawn framing camera images. Planet. Space Sci. 129, 103–107.
Ruesch, O., et al., 2016. Cryovolcanism on Ceres. Science 353.
Russell, C.T., Raymond, C.A., 2011. The Dawn mission to vesta and Ceres. Space Sci. Rev. 163, 3–23.
Schmedemann, N., et al., 2017. The Distribution of Impact Ejecta on Ceres. Lunar Plan. Sci., The Woodlands, TX.
Schmidt, R.M., Housen, K.R., 1987. Some recent advances in the scaling of impact and explosion cratering. Int. J. Impact Eng. 5, 543–560.
Schorghofer, N., et al., 2016. The permanently shadowed regions of dwarf planet Ceres. Geophys. Res. Lett. 43, 6783–6789.
Schröder, S.E., et al., 2016. Boulders on Ceres. EGU (abstract).
Schultz, P.H., Ernst, C.M., Anderson, J.L., 2005. Expectations for Crater Size and Photometric Evolution from the Deep Impact Collision. Deep Impact Mission: Looking beneath the Surface of a Cometary Nucleus. Springer, pp. 207–239.
Schultz, P.H., Wrobel, K.E., 2012. The oblique impact Hale and its consequences on Mars. J. Geophys. Res.: Plan 117 n/a-n/a).
Shoemaker, E.M., 1962. Interpretation of lunar craters. Physics and Astronomy of the Moon 283–359.
Shoemaker, E.M., 1965. 2. Preliminary analysis of the fine structure of the lunar surface in mare cognitum. Int. Astron. Union Circular 5, 23–77.
Thomas, P., Veverka, J., Robinson, M., Murchie, S., 2001. Shoemaker crater as the source of most ejecta blocks on the asteroid 433 Eros. Nature 413, 394.
Thomas, P., et al., 2000. Phobos: regolith and ejecta blocks investigated with Mars orbiter camera images. J. Geophys. Res.: Plan 105, 15091–15106.
Thomas, P.C., et al., 2005. Differentiation of the asteroid Ceres as revealed by its shape. Nature 437, 224–226.
Vickery, A., 1986. Size-velocity distribution of large ejecta fragments. Icarus 67, 224–236.
VoT.H, P., Czygan, M., Kumar, A., Raman, K., 2017. Python: Data Analytics and Visualization. Packt Publishing, Birmingham.
Weibull, W., 1951. Wide applicability. J. Appl. Mech. 103, 293–297.
Werner, S.C., Ivanov, B.A., 2015. 10.10-Exogenic Dynamics, Cratering, and Surface Ages A2-schubert, Gerald. Treatise on Geophysics, second ed. Elsevier, Oxford, pp. 327–365.
Werner, S.C., Ivanov, B.A., Neukum, G., 2009. Theoretical analysis of secondary cratering on Mars and an image-based study on the Cerberus Plains. Icarus 200, 406–417.
Wieczorek, M.A., Zuber, M.T., 2001. A Serenitatis origin for the Imbrian grooves and South Pole-Aitken thorium anomaly. J. Geophys. Res. Plan 106, 27853–27864.
Wilhelms, D., Oberbeck, V., Aggarwal, H., 1978. Size-frequency distributions of primary and secondary lunar impact craters. Lunar and Planetary Science Conference Proceedings 9, 3735–3762.
Wilson, L., Head, J.W., 2015. Groove formation on Phobos: testing the Stickney ejecta emplacement model for a subset of the groove population. Planet. Space Sci. 105, 26–42.
Wrobel, K.E., 2004. Effect of planetary rotation on distal tektite deposition on Mars. J. Geophys. Res. 109.